

Crack propagation in fine grained graphites under mode I and mixed-mode loading, as observed in situ by microtomography

Xiaochao Jin ^{a, b}, T. James Marrow ^{b, *}, Jierui Wang ^a, Yang Chen ^b, Hongniao Chen ^{b, c}, Daniel Scotson ^b, Boyuan Wang ^a, Houzheng Wu ^d, Xueling Fan ^{a, **}

^a State Key Laboratory for Strength and Vibration of Mechanical Structures, School of Aerospace Engineering, Xi'an Jiaotong University, Xi'an, 710049, China

^b Department of Materials, University of Oxford, Parks Rd, Oxford, OX1 3PH, UK

^c Space Structures Research Center, Guizhou University, Guiyang, 550525, China

^d Department of Materials, Loughborough University, Epinal Way, Loughborough, LE11 3TU, UK

ARTICLE INFO

Article history:

Received 16 September 2021

Received in revised form

17 March 2022

Accepted 20 March 2022

Available online 21 March 2022

Keywords:

Graphite

Fracture toughness

Stress intensity factor

Mixed mode

Diametral compression

X-ray computed tomography

ABSTRACT

Stable crack growth under mode I and mixed-mode loading of two fine grained advanced graphites, SNG742 and T220, has been studied within small (18 mm diameter) specimens of the diametral compression disc geometry to investigate the criterion for crack propagation. Cracks were propagated from a central notch, inclined at 0° or 30° to the loading axis, as the tests were observed in situ by X-ray computed microtomography. The three-dimensional (3D) displacement fields were measured by digital volume correlation. The crack shape, tip location and crack opening displacements were determined by 3D phase congruency edge detection of full field displacements. Linear elastic 3D finite element simulations calculated the J-integral and mode I, mode II and mode III stress intensity factors (SIFs) acting on the crack tip, using the full field displacements as boundary conditions. For SNG742 and T220 specimens with notch angle of 0°, nearly pure mode I crack propagation was obtained. For specimens loaded with the 30° notch angle, the SIFs changed from mixed mode I/II towards pure mode I as the crack propagated. The mode II SIF was less than 20% of the mode I SIF, and as the crack extended over a distance ~3 mm, the critical mode I SIF (fracture toughness) was insensitive to the mode II SIF, with SNG742 graphite having higher fracture toughness than T220 graphite.

© 2022 The Authors. Published by Elsevier Ltd. This is an open access article under the CC BY license (<http://creativecommons.org/licenses/by/4.0/>).

1. Introduction

Graphite is an important nuclear material. It is used in the core of the current Advanced Gas-cooled Reactors (AGR) [1,2] as a neutron moderator and reflector, and also acts as a structural component providing channels for the coolant gas, fuel, control rods and shutdown devices [3,4]. Advanced graphites are candidate materials for the moderator and structural components in some designs of Generation IV advanced reactors [5,6]. These are load-bearing components, keyed in a structure that forms the reactor core. The integrity of the graphite components is critical to the safe operation of these reactors [7]. In addition to self-weight loads, the graphite components are subject to complex loads from

irradiation-induced shrinkage and thermal stresses over the life of the reactor, as well as restraint loads and possible seismic loads. These loads have the potential to cause fracture, and significant damage to the core may affect its safe operation [8–12]. Understanding and knowledge of the properties of graphite are needed to forecast the risk of fracture, especially the criteria for crack initiation and propagation under different stress states. To support the structural integrity assessment and design of graphite components, and for management of the reactor lifetime [13,14], this requires knowledge of the fracture toughness of irradiated graphite under different states of loading.

The fracture toughness of nuclear graphite is generally obtained from large (10's of cm³) standardised specimens [15]. Irradiated graphite can only be obtained from operating power reactors, or materials test reactors, and there is a need to obtain reliable and conservative data from smaller test specimens that require less material [16–18]. The double-cleavage drilled compression (DCDC) geometry is one that is suitable for small specimen tests of graphite

* Corresponding author.

** Corresponding author.

E-mail addresses: james.marrow@materials.ox.ac.uk (T.J. Marrow), fanxueling@mail.xjtu.edu.cn (X. Fan).

[19]. It was recently used in a study of the mode I fracture toughness in irradiated graphite [20], and sufficient crack propagation could be achieved to examine the R-curve behaviour (i.e., rising fracture toughness with increasing crack length) that has also been observed in larger specimens of unirradiated graphite [21–23]. In the DCDC specimen, longitudinal compression induces a transverse tensile stress that can drive stable propagation of cracks, which initiate at stress concentrating notches from the central drilled hole. Direct observation of the applied stress and crack length is then used to obtain the critical mode I stress intensity factor (SIF) for quasi-static crack propagation, i.e., the fracture toughness, K_{Ic} . However, the analytical SIF solution for the DCDC specimen makes assumptions of the boundary conditions, which can lead to significant errors in small test specimens [24], and there is currently no standard to provide guidance on its limitations. The same issues may arise in other small specimens, such as the centre-cracked or centre-notched diametral compression test that may be used to investigate fracture under mixed mode loading [25,26], for which the DCDC specimen is not suitable.

To address this challenge, a novel analysis method has been developed [24,27–29], which makes use of direct measurements of the local boundary conditions, i.e., the displacement field around the crack, to extract the local SIF for small specimens. Three-dimensional (3D) observations of deformation and damage can be obtained by in situ high-resolution X-ray computed tomography (XCT), and attenuation contrast from the porous graphite microstructure allows use of digital volume correlation (DVC) to map the relative changes in the displacement field between tomographic datasets. Using this information, finite element simulations can calculate the elastic strain energy release rate (J-integral), and under small-scale yielding conditions (i.e., linear elasticity), the local mode I, II and III SIFs acting on the crack tip can be obtained.

Most investigations of the fracture behaviour of nuclear graphite have focused on pure mode I loading. Due to the complex geometry of graphite components [30] and the development of 3D stress states from dimensional change [31], cracks may propagate from stress concentrating notches under mixed mode loading [32]. Kinked or branched cracks may also develop [33,34] and may experience mixed mode loading at the crack tip. To date, relatively few studies of graphite fracture have been carried out under mode II or mixed mode loading conditions [35–42], with emphasis on the criteria for initiation of fracture from the stress concentration of a notch. The crack propagation resistance of brittle materials can be affected by mixed mode loading [43,44], and both microstructural size and specimen geometry are important factors [45,46]. Due to the heterogeneous structure of the medium to coarse grained graphites used in the AGRs [23], cracks propagate with a rough fracture surface that has been shown to contribute to the R-curve development. The effect of fracture surface roughness at the microstructural length scale has also been shown to be important in studies of mixed mode fracture propagation in concrete and coarse-grained graphite [47,48]. It is unclear, however, whether the fracture toughness of fine-grained advanced graphites is similarly affected by the mode of loading. This is important in order to be able to assess the propagation (i.e., crack path and potential for crack arrest) of fractures that may initiate at stress concentrations and other material defects under the influence of the complex stress fields from thermal and irradiation dimensional change.

In this work, stable crack propagation in two fine-grained advanced graphites, SNG742 and T220, has been studied. The long term motivation of this study is the development of experimental techniques to investigate the fracture properties of neutron-irradiated graphite. There are significant limitations on specimen size in that case, imposed by the availability of space in materials test reactors or the dimensions of materials that can be

removed from operating reactors. Before conducting studies of irradiated graphites, the experimental and analysis methods must be developed on non-irradiated materials. For this purpose, we have chosen the diametral compression disc specimen with a central stress concentrating notch, as this geometry has potential to be used for testing of small specimens of irradiated graphite and may also achieve mixed mode conditions.

To obtain mode I and mixed modes I/II, the compressive load was applied in two different configurations of diametral compression disc specimens with the initiating notch inclined at 0° or 30° to the loading axis. The tests were observed in situ by XCT, with the 3D displacement fields measured by DVC. The diametral compression disc specimen with centre-notch is generally used to study crack propagation of materials with observations of the two-dimensional specimen surface. However, this makes the assumption that the crack tip that is observed on the surface is fully representative of the crack front within the specimen. The XCT observations have tested this assumption in this work, and show that irregular crack propagation can occur with variation of the crack length across the specimen width. In this work, the crack tip location and crack opening displacements were determined using edge detection of the phase congruency of the displacement field. Finite element simulations were then performed using only these measured local boundary conditions to obtain the elastic strain energy release rate as the J-integral, from which the magnitudes of the SIFs acting locally on the crack tip were extracted using the interaction integral. The objective was to measure the crack propagation criteria in fine-grained SNG742 and T220 graphites under different modes of loading, without assumptions that depend on knowledge of the specimen geometry, crack length and load.

2. Experiments and analysis methods

2.1. Materials and experiments

The materials examined are both candidate fine grained poly-granular graphites for advanced nuclear fission reactors. SNG742 is proposed for very high temperature reactors and has a coke size around 20 μm [49] with a mass density of 1.83 g cm^{-3} [50]. T220 is an ultrafine grain graphite grade for molten salt experimental reactors with an average coke size of around 5 μm and a density of 1.85–1.87 g cm^{-3} [51,52]. The fracture toughness values of SNG742 and T220 have been reported to be 1.12 $\text{MPa m}^{1/2}$ [49] and 0.8–1 $\text{MPa m}^{1/2}$ [53] respectively. The material was in the virgin condition (i.e., not irradiated).

The SNG742 and T220 graphite specimens were machined to a disc that was 18 mm diameter and 9 mm thickness. A through-thickness central hole (2 mm diameter) was drilled and aligned with the axial Z-direction, and a through-thickness notch (total length 4 mm, width 1 mm, tip radius 0.5 mm) was cut along the disc diameter (Fig. 1a). The in situ micro-computed tomography (μXCT) tests were performed within a Zeiss Xradia 510 Versa x-ray microscope, with the uniaxial compressive load applied along the vertical Y-direction using a 5 kN Deben H250 loading device (Deben UK Ltd, Suffolk, UK). To study the crack propagation behaviour under I and II mixed modes, the compressive loads were applied with the centre notch aligned at 0° (configuration 1) and 30° (configuration 2) with respect to the loading Y-axis (Fig. 1a). In configuration 2, the expected ratio of mode I to mode II SIF for a 30° inclined sharp crack is about 0.05 [49,54–56]. To prevent fracture initiation from the stress concentration of the loading contact, arc shaped high-strength aluminum alloy anvils [33] (radius 18 mm) with a load-bearing sector angle of 30° were used.

Tomographs were recorded at intervals as the load was increased, from a pre-load of ~20 N, with the applied cross-head

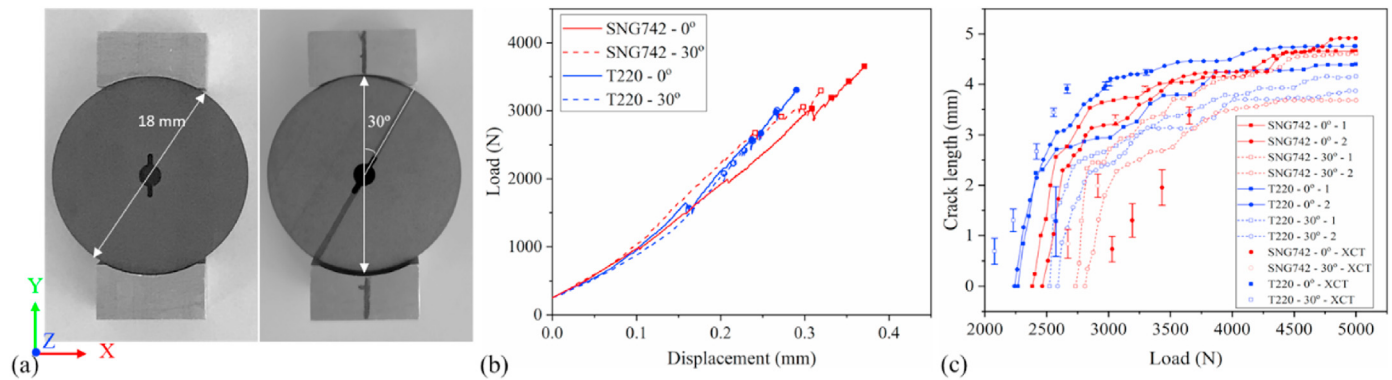


Fig. 1. Diametral compression disc specimens with central-notch: (a) 0° and 30° configurations; (b) load vs cross-head displacement for the in situ XCT study with points marking the recording of tomographs; (c) crack length (Y direction) vs load, for optical surface observations (additional specimens) and XCT observations (the error bars show the range of crack lengths of the XCT observations over a central 7 mm region). (A colour version of this figure can be viewed online.)

displacement constant during the tomography (Fig. 1b). The tomographs were obtained with 1601 radiographic projections over a 180° rotation, each with a field of view of 11.7×11.5 mm (2048×2008 pixels at an effective pixel size of $5.72 \mu\text{m}$) and 40 s exposure time (70 kV and 6 W power) [Supplementary Information, section 1]. A small load relaxation (typically less than ~ 60 N) was observed during each tomograph (duration ~ 18 h). The attenuation contrast tomographs were reconstructed using the instrument software.

A series of tests using the same anvils was performed with in situ optical observations of the specimen surface, to check that the specimens observed by in situ μXCT behaved similarly. The compressive load was applied at a displacement rate of 0.1 mm/min using a 5000 N Shimadzu loading rig. To improve the surface contrast of the specimens, a speckle pattern was applied using an airbrush (black speckle on white background). One surface of each specimen was observed using a GOM ARAMIS 5 M (5-megapixels) two-camera system (Titanar 75 mm lens with NOGA LED illumination) to record images at 10 frames per second. For the SNG742 and T220, 2 specimens of each graphite type were tested under each loading configuration, (8 specimens in total). The crack length (vertical distance in Y-direction from notch tip to crack tip) was measured by inspection of the camera images, without the need for image correlation analysis. Crack propagation was similar from each notch tip, and only one set of crack length measurements is reported for each specimen (Fig. 1c). No further analysis of these specimens has been done, as the surface crack length cannot be assumed to be representative of the crack length across the specimen thickness.

2.2. Digital volume correlation analysis

The reconstructed tomography images were converted from 16-bit to 8-bit using ImageJ before the digital volume correlation (DVC) analysis, which was performed with the LaVision DaVis software (version 8.4.0) using a procedure that combined an initial FFT (Fast Fourier Transform) correlation and then a series of multi-pass direct correlations. The pre-load tomograph was used as reference for all analyses of the region around the crack that was cropped to dimensions (X \times Y \times Z) of $1080 \times 960 \times 1200$ voxels ($6.18 \times 5.49 \times 6.86$ mm). For each loading step, two independent analyses were performed using subset sizes of $32 \times 32 \times 32$ voxels and $96 \times 96 \times 96$ voxels respectively (voxel dimension: $5.72 \mu\text{m}$), both with an overlap of 75% between subsets. A correlation coefficient threshold of 0.75 was imposed with any invalid displacement vectors being deleted.

2.3. 3D crack characterization

Phase Congruency (PC), which is a displacement-based method that uses a 3D edge detection algorithm to detect the discontinuity of the crack surface, was applied to extract the crack tip position and to measure the crack opening displacements from the DVC data [27,30]. For improved spatial resolution, the PC analysis was performed with the 32^3 voxel subset data, which had a grid spacing of $\sim 46 \mu\text{m}$ between displacement vectors. The nominal mode I, mode II and mode III crack opening displacements (COD), parallel to the X, Y and Z directions, were obtained from the differences between the displacement vectors on opposing sides of the crack (dUx, dUy and dUz, respectively).

2.4. Finite element analysis

The purpose of the finite element analysis is to calculate the stress field within the observed field of view, by using the measured displacement field as the local boundary condition. The 3D finite element analysis was performed using the Abaqus software (version 6.14), with a model established using the same dimensions as the cropped tomography data (i.e. $\sim 6 \times \sim 6 \times \sim 7$ mm). The crack was simplified either as a planar (Y-Z plane) surface for configuration 1 (0°), or 3D curved surface for configuration 2 (30°), with the crack tip locus determined by the PC analysis [Supplementary Information, section 2]. Each point of the identified crack tip was an element node, and the mesh in the vicinity of crack was refined as in previous work that used DCDC specimens [57]. The 3D displacement field, measured using the DVC analysis with 96^3 subset size, was injected into the simulation model as the boundary conditions. A set of “forbidden nodes” was defined that included the nodes in the vicinity of the crack where the DVC correlation coefficient was low [28,57]. The displacements at the forbidden nodes, and other nodes with no injected DVC displacement, were calculated within the FE solver using the surrounding nodal displacements and the free surface of the crack as boundary conditions [57], by satisfying the continuity and compatibility conditions for static equilibrium. With the assumption of linear elasticity, the J-integral strain energy release rate and local stress intensity factors (SIFs) under mode I, mode II and mode III were then obtained in the frame of reference of the local crack path (i.e., for a virtual crack extension in the direction within the X–Y plane that is defined by the tangent to the crack) using the interaction integral method that is implemented within Abaqus/Standard [Supplementary Information, section 3]. In the simulations, the elastic modulus and Poisson's ratio of the two graphites are both taken as 11.0 GPa and 0.2, respectively, which are typical for fine-grained graphite [50].

3. Results

In this section, the results of DVC analysis are first presented, from which the characteristic dimensions of the cracks are extracted via an analysis of the phase congruency of the 3D displacement field. The strain energy release rate and SIFs are then obtained using linear elastic finite element analysis, with the measured displacement fields as boundary conditions.

3.1. DVC analysis

To estimate the uncertainty in the DVC measurement of displacements, the standard deviation of the displacements was measured in a region remote ($Y = 3.0$ mm, $Z = 3.2$) from the notch, where the strain was small. In a representative SNG742 specimen, using data for the test in the 0° configuration at 3029 N load, with subsets of 32^3 and 96^3 voxel, the standard deviations of the displacements ($n = 134$ and 45 , respectively) were similar at 3.6 and 3.5 μm (0.63 and 0.61 voxel), respectively.

Crack propagation in SNG742 and T220 specimens with the 0° configuration is illustrated in Fig. 2, using 2D slices of the 3D tomographs and maximum normal 3D strain, calculated in the DVC software from the gradient of the displacement field using data from the higher spatial resolution 32^3 voxel subset analysis. The maps show the same X–Y plane near the centre of each specimen ($Z = 3.43$ mm, where $Z = 0$ is 1 mm from the specimen surface). The crack in the XCT image (bounded by the magenta dashed box) is quite consistent with the strain visualization, where the strain is due to the discontinuity in the displacement field from the crack

opening. The crack propagated parallel to the Y-axis, as expected for the mode I loading of this configuration. The displacement fields measured for the same specimens by the DVC analysis with 96^3 voxel subset size are presented in Fig. 3 for the displacement components in the X, Y and Z directions of the central X–Y plane (U_x, U_y, U_z). These also show the discontinuity of the crack opening in the X direction. Since manual registration of the datasets was done before the DVC analyses, only small rigid body movements (maximum 38 μm) of the specimens during the loading process can be observed. The development of the crack from one notch in the 30° configuration is similarly shown in Figs. 4 and 5 for the SNG742 and T220 specimens. In both, the crack propagated to become parallel to the vertical plane, having initiated at an angle of approximately 55° from the notch plane towards the vertical plane; i.e. the crack did not initiate parallel to the inclined central notch. This was also observed in the optical observations of all specimens tested in the 30° configuration. Similar behaviour has been observed in mixed mode testing of notched specimens of brittle materials [58]. It is due to the development of maximum tangential stress at this location, the calculation of which, with necessary assumptions such as a critical microstructure length scale, has been used previously to obtain critical mode I and mode II stress intensity factors [49,58].

3.2. Crack length and crack opening

The tomographs and their DVC and phase congruency analyses are used to provide data on the crack shape and geometry at each stage in the experiments. Any change in crack length during the recording of

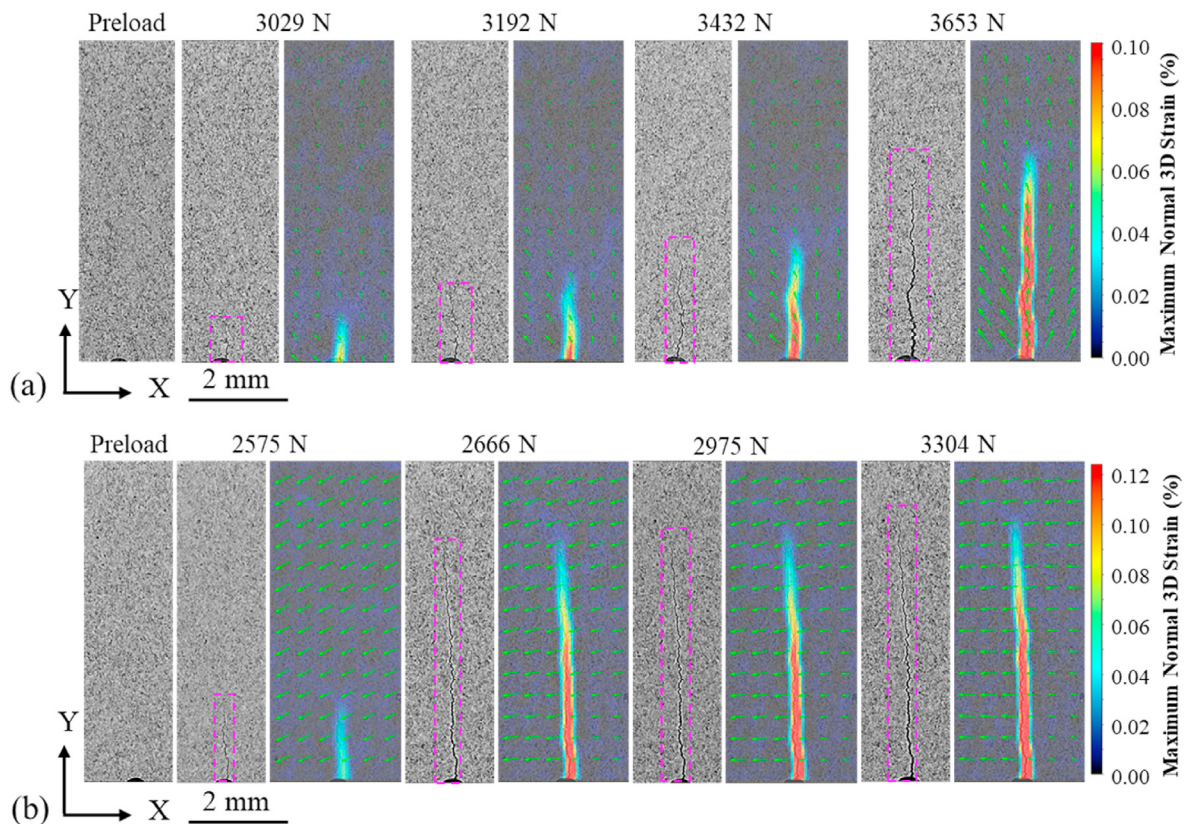


Fig. 2. XCT visualization of the crack as it propagates with increasing load in (a) SNG742 and (b) T220 in the 0° configuration. The crack is visualised in virtual slices and with contour maps of maximum normal 3D strain in the X–Y plane near the centre of the specimen. The magenta dashed box in the tomographs marks the extent of the visible crack. The green arrows show the direction and magnitude of the displacements in the X–Y plane, relative to the preloaded tomograph. (A colour version of this figure can be viewed online.)

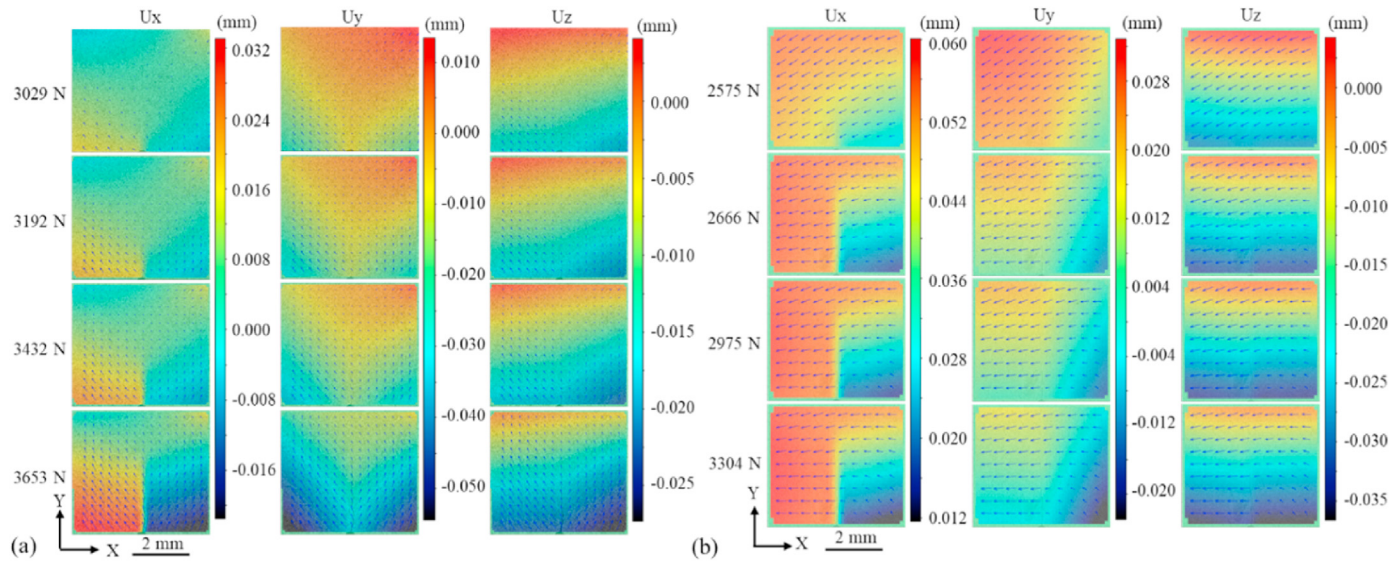


Fig. 3. The evolution of the displacement fields with increasing load of (a) SNG742 and (b) T220 in the 0° configuration, measured by DVC and presented on an X–Y plane near the specimen centre. The dark arrows represent the displacement vectors in the X–Y plane, and the colour contours show the displacements (mm) in the X, Y and Z directions (Ux, Uy and Uz), relative to the preloaded tomograph. (A colour version of this figure can be viewed online.)

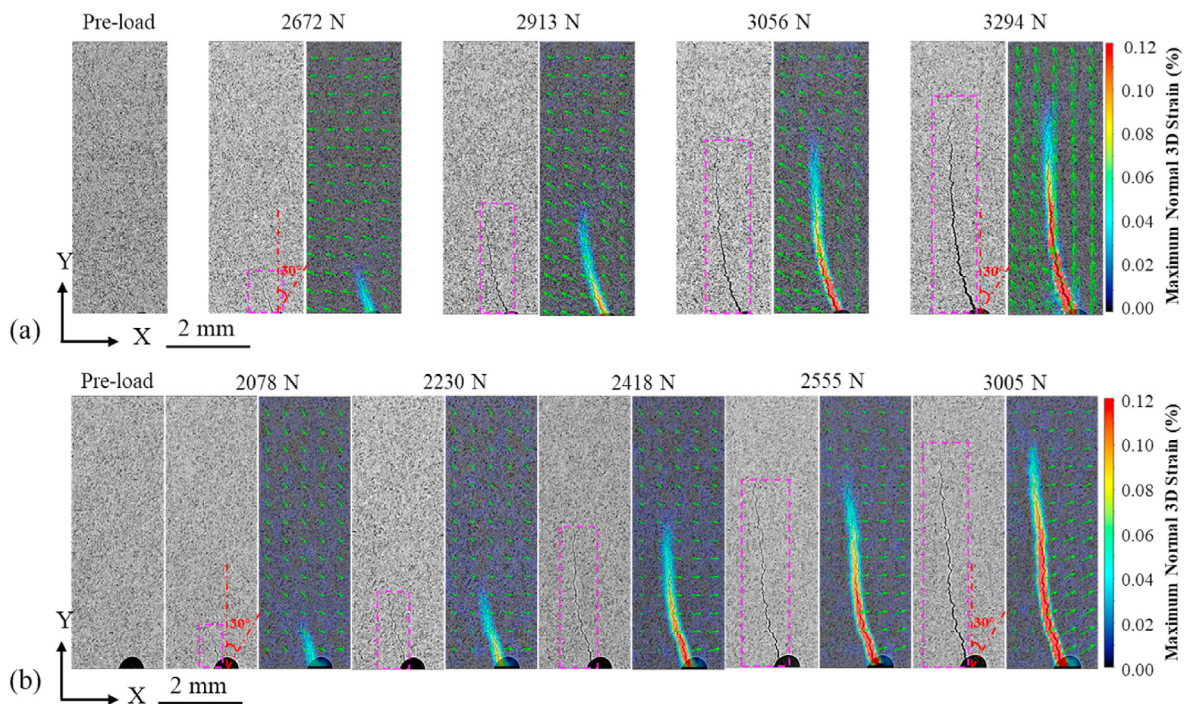


Fig. 4. XCT visualization of the crack as it propagates with increasing load in the (a) SNG742 and (b) T220 in the 30° configuration. The crack is visualised in virtual slices and with contour maps of maximum normal 3D strain in the X–Y plane near the centre of the specimen. The red dashed box in the tomographs marks the extent of the visible crack. The green arrows show the direction and magnitude of the displacements in the X–Y plane, relative to the preloaded tomograph. (A colour version of this figure can be viewed online.)

the tomographs would cause movements of the specimen, and if larger than a few voxels would blur the reconstructed tomograph. No such blurring occurred, so significant crack propagation did not occur during the recording of the tomographs. The strain field can be used to visualise the crack by choice of a suitable strain threshold, but a more objective assessment of the crack tip location can be obtained using phase congruency analysis of the displacement field [24,27]. The evolution of the crack tip position of the four specimens, measured at positions across the analysed ~7 mm central region of the 9 mm

specimen thickness (Z-direction), is presented in Fig. 6. The crack lengths are presented as the vertical distance in the Y-direction from the notch to the crack tip. Data for the averaged crack length (~150 data points across the thickness in each case) are listed in Table 1 and presented in Fig. 1c. The crack fronts are quite smooth, but are not initially uniform, particularly in T220 in the 0° configuration where the crack lengths approaching the specimen's free surfaces differ quite significantly. The crack front tends to become more uniform across the thickness with increasing load. This non-uniformity may be

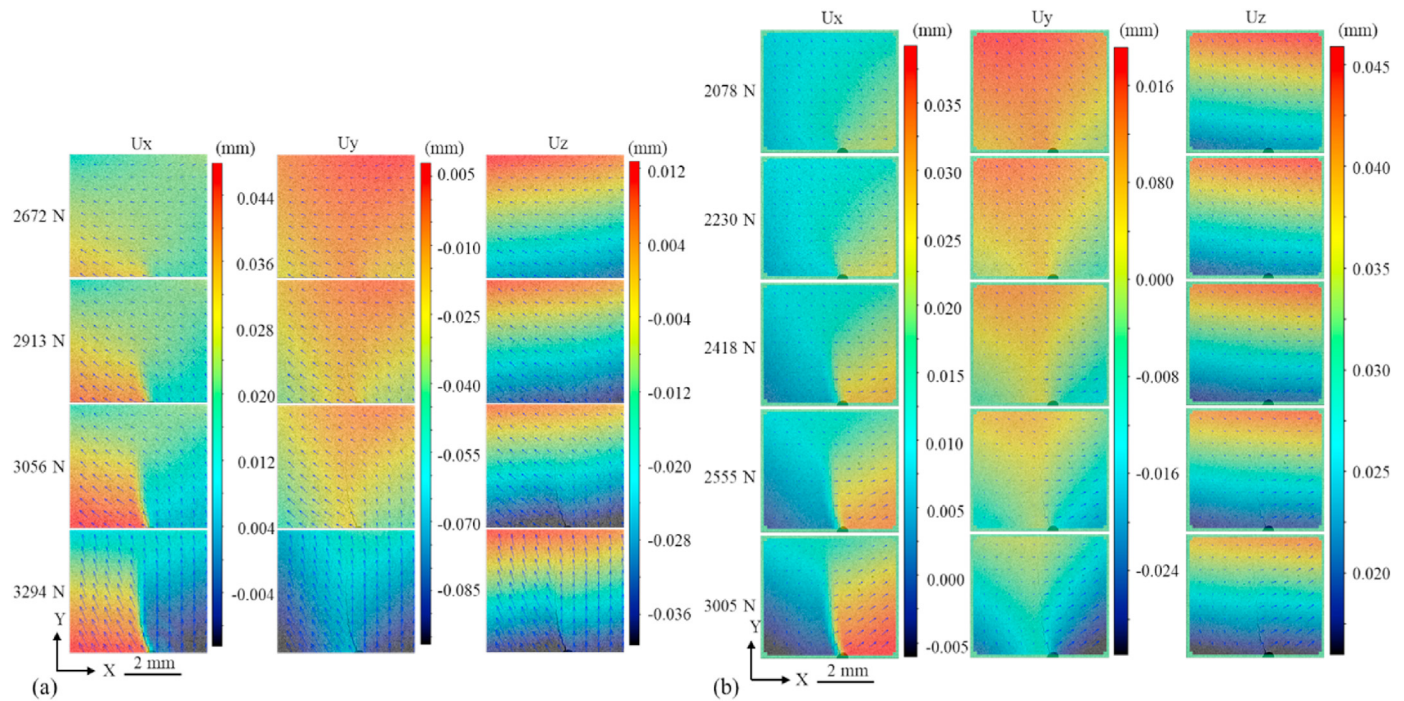


Fig. 5. The evolution of the displacement fields with increasing load of (a) SNG742 and (b) T220 in the 30° configuration, measured by DVC and presented on an X–Y plane near the specimen centre. The blue arrows represent the displacement vectors in the X–Y plane, and the colour contours show the displacements (mm) in the X, Y and Z directions (Ux, Uy and Uz), relative to the preloaded tomograph. (A colour version of this figure can be viewed online.)

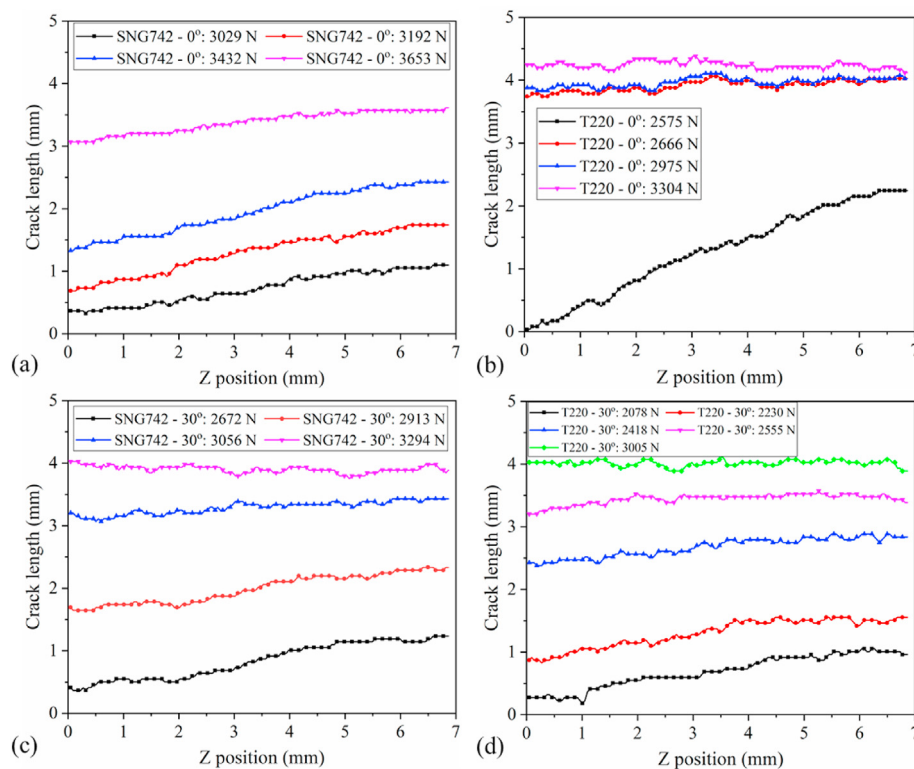


Fig. 6. The variation of the crack length across the specimen at different loads: (a) and (b) SNG742 and T220 in the 0° configuration, (c) and (d) SNG742 and T220 in the 30° configuration. The data are obtained by PC analysis of the μ XCT images. For clarity, only one third of the data points are shown. (A colour version of this figure can be viewed online.)

due to imperfect alignment of the compression of the specimens in the XCT loading rig, and it is noticeable that the lengths of the XCT observed cracks differ from the surface lengths of the optically

observed specimens (Fig. 1c) that were loaded in the conventional rig. Nonetheless, the general behaviours of the XCT and optically observed specimens are quite similar.

Table 1

The development of the crack length and opening angle in the SNG742 and T220 graphite specimens with load. Each data for the length is the average of about 150 measurements over the crack front.

Graphite-configuration	Load (N)	crack length (MM)	Crack opening angle (°)	Graphite-configuration	Load (N)	crack length (MM)	Crack opening angle (°)
SNG742-0°	3029	0.73 ± 0.25	0.31	SNG742-30°	2672	0.84 ± 0.29	0.31
	3192	1.30 ± 0.33	0.29		2913	1.99 ± 0.23	0.29
	3432	1.95 ± 0.35	0.29		3056	3.29 ± 0.10	0.26
	3653	3.38 ± 0.17	0.40		3294	3.90 ± 0.06	0.36
T220-0°	2575	1.28 ± 0.69	0.22	T220-30°	2078	0.69 ± 0.26	0.22
	2666	3.91 ± 0.09	0.24		2230	1.30 ± 0.22	0.24
	2975	3.97 ± 0.08	0.25		2418	2.67 ± 0.15	0.24
	3304	4.24 ± 0.05	0.27		2555	3.44 ± 0.08	0.25
					3005	4.01 ± 0.05	0.31

Maps of the crack opening displacements (COD) are presented in Figs. 7 and 8. The mode I displacements are most significant, and the cracks open more evenly across the specimen thickness with increasing load. The mode II and mode III displacements are small in comparison to the mode I displacements for the 0° configuration, but in particular for mode II these displacements are more significant in the 30° configuration. These displacements are measured in the XYZ frame of reference of the loading, and do not consider the local path of the crack; however, due to the near-vertical crack paths the effect of this is not substantial.

The crack opening behaviour of SNG742 and T220 in the 0° configuration is further illustrated in Fig. 9, using the mode I COD, averaged over the analysed thickness. This is presented as a function of distance from the position where the average COD became zero (i.e., the furthest extent of the crack tip). Its gradient provides a measure of the average crack opening angle, which tends to increase as the crack length increases at the higher loads. The crack opening angles (Table 1) are similar in both the 0° and 30° configurations, and are higher for SNG742 than T220. The average mode II COD values of SNG742 and T220 in the 30° configuration are also illustrated in Fig. 10. The mode II COD was very small and did not vary significantly with crack growth for the 0° configuration, while in the 30° configuration the larger mode II COD tended to decrease and then saturate with increasing load as the crack grew.

The mode I displacements at the crack mouth (CMOD) are compared with the mode II and mode III values in Fig. 11 as a function of crack length. In the 0° configuration, the mode I CMOD increased with crack length, while the mode II and mode III CMODs

were negligible for both graphites. In the 30° configuration, both the mode I and mode II CMOD increased with crack length with similar average ratios of 2.1 ± 0.3 and 2.5 ± 0.7 for SNG742 and T220, respectively, whereas the mode III CMOD remained small in comparison.

The local SIFs (K_I , K_{II} and K_{III} for modes I, II and III, respectively), were extracted directly from the J-integral in Abaqus at 31 equally spaced points along the analysed crack front. These values are presented in Fig. 12 with the local crack length (i.e., the crack length at the measurement position). For both SNG742 and T220 in the 0° configuration, the average K_I was constant with crack length at 1.54 ± 0.13 and 1.40 ± 0.13 MPa m^{1/2}, respectively (mean ± standard deviation). In the 30° configuration, the average K_I was constant for crack length up to ~3 mm, with values of 1.50 ± 0.17 and 1.43 ± 0.12 MPa m^{1/2} for SNG742 and T220. However, for longer crack lengths the average K_I of SNG742 and T220 graphite increased to 2.11 ± 0.34 and 1.93 ± 0.19 MPa m^{1/2}, respectively. The ratio K_{II} : K_I was low at <0.2 for both the 0° and 30° configurations. Except for the longest crack lengths, K_{III} was small in comparison.

4. Discussion

The fracture toughness of quasi-brittle materials such as polygranular graphite can be size dependent [59,60], with the development of an R-curve with increasing crack length [61,62]. In this work, which aims to develop a fracture test method that can be applied to small specimens, the J-integral and SIFs are not calculated using conventional fracture analyses that use the load and geometry parameters as inputs to calculate the stress and strain

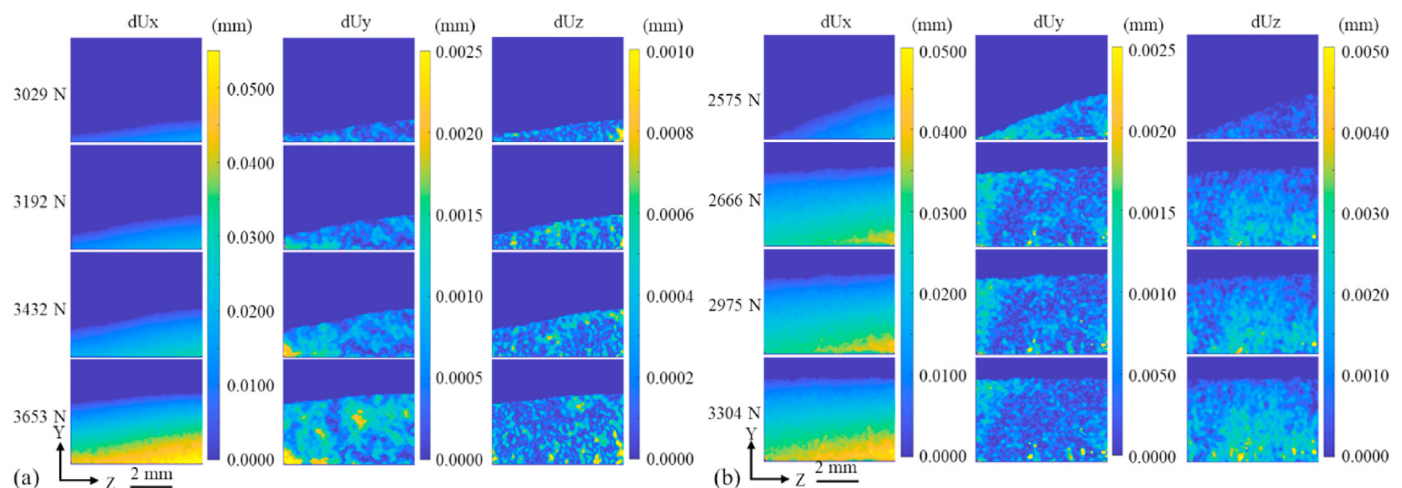


Fig. 7. Maps of the crack opening displacements in the (a) SNG742 and (b) T220 in the 0° configuration, measured in the X (mode I: dUx), Y (mode II: dUy) and Z (mode III: dUz) directions, as a function of the applied load. The crack propagates from bottom to top. (A colour version of this figure can be viewed online.)

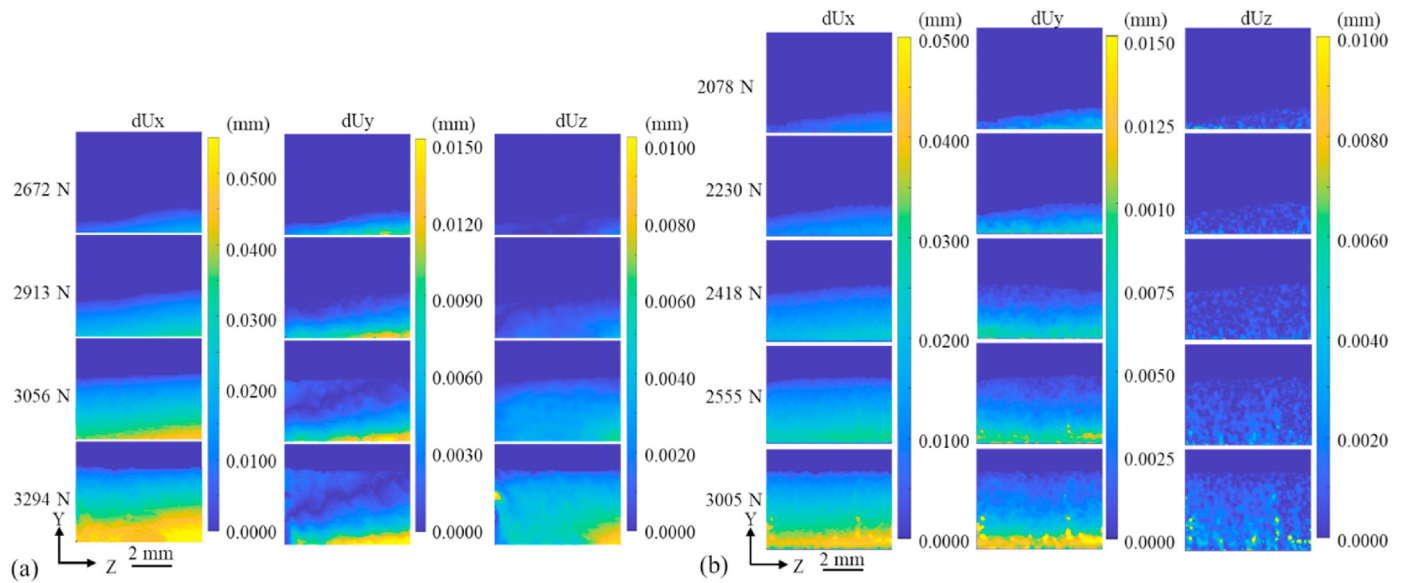


Fig. 8. Maps of the crack opening displacements in the (a) SNG742 and (b) T220 in the 30° configuration, measured in the X (mode I: dUx), Y (mode II: dUy) and Z (mode III: dUz) directions, as a function of the applied load. The crack propagates from bottom to top. (A colour version of this figure can be viewed online.)

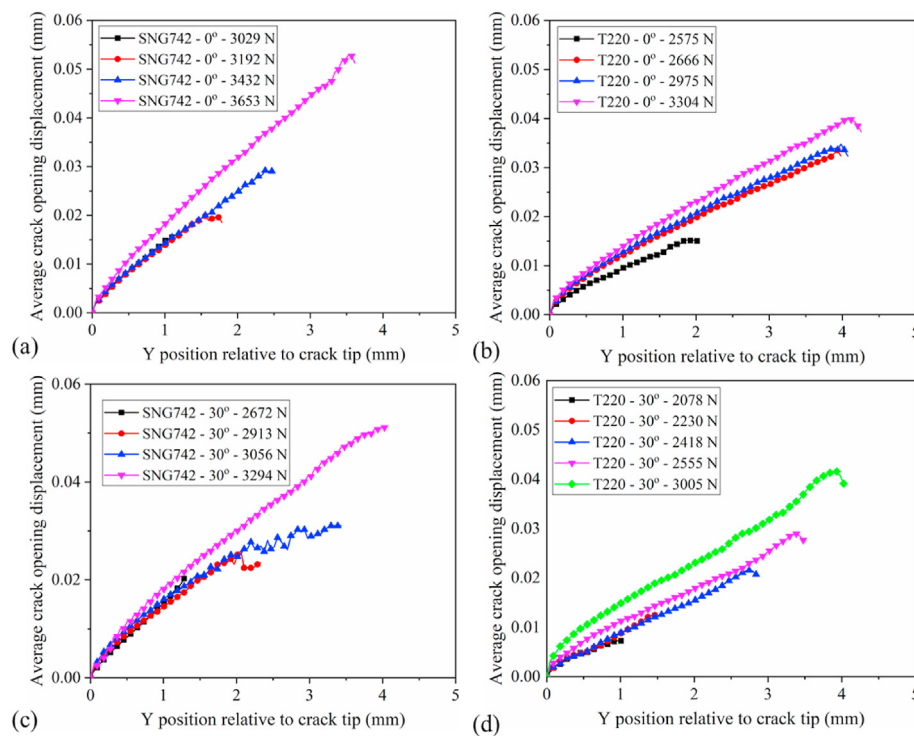


Fig. 9. The mode I crack opening displacements (dUx) averaged across the specimen thickness, as a function of the Y-distance from the average position of the crack tip: (a) and (b) SNG742 and T220 in the 0° configuration, (c) and (d) SNG742 and T220 in the 30° configuration. (A colour version of this figure can be viewed online.)

energy fields. Here, the critical SIFs of quasi-static propagating cracks are calculated by FE simulations that use the displacement fields measured from the DVC analysis as local boundary conditions. This method is independent of the effects of load and the geometry and size of the specimen. However, the extent of crack propagation is limited by the small size of the test specimen, which is imposed by the longer term objective to study irradiated graphites. Such small specimens may not develop sufficient crack propagation to establish an R-curve, but data for short crack

extensions would provide a conservative measure of the fracture toughness.

For both SNG742 and T220 in the 30° configuration, as shown in Fig. 12, the average K_I is quite close to the corresponding value for the same graphite in the 0° configuration and much larger than K_{II} . In the 30° configuration, K_{II} at the crack tip was small (<20% of K_I), despite the shear loading of the central notch that was revealed by the higher ratios (~40–50%) of the CMOD values for shear and opening. The smaller mode II SIF may be due to fracture surface

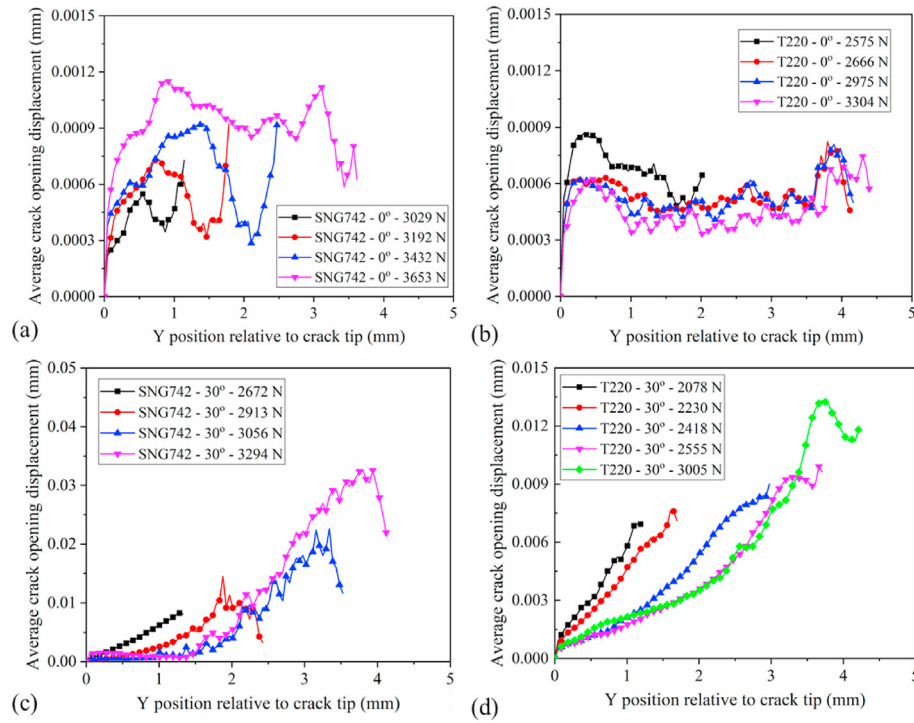


Fig. 10. The mode II crack opening displacements (dU_y) averaged across the specimen thickness, as a function of the Y-distance from the average position of the crack tip: (a) and (b) SNG742 and T220 in the 0° configuration, (c) and (d) SNG742 and T220 in the 30° configuration. (A colour version of this figure can be viewed online.)

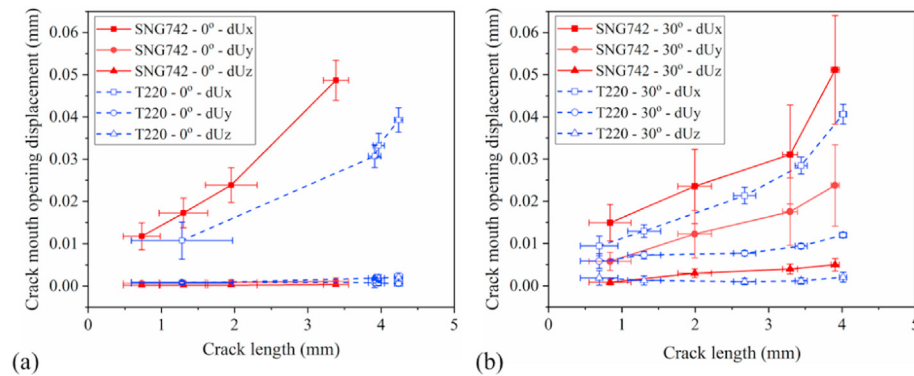


Fig. 11. The average components of the crack mouth opening displacements (mode I: dU_x , mode II: dU_y and mode III: dU_z) as a function of average crack length. (a) SNG742 and T220 in the 0° configuration, (b) SNG742 and T220 in the 30° configuration. The error bars are the standard deviations. (A colour version of this figure can be viewed online.)

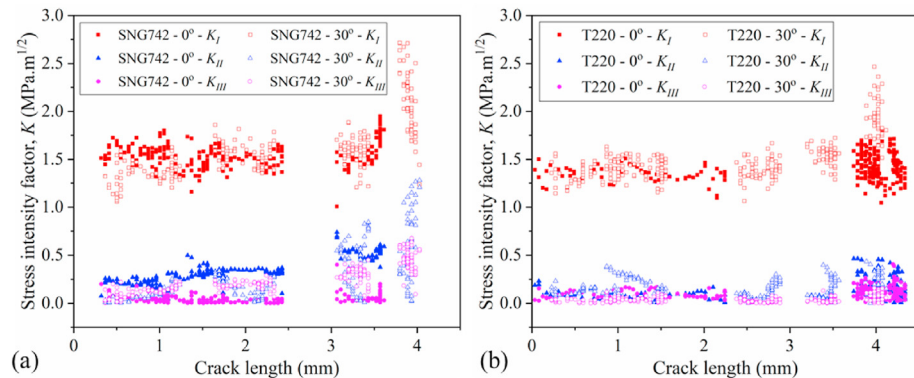


Fig. 12. The stress intensity factors (K_I , K_{II} and K_{III}) at all positions over the crack front, as a function of the local crack length in the 0° and 30° configurations for (a) SNG742 and (b) T220 graphites. (A colour version of this figure can be viewed online.)

roughness, which can act to reduce the shear displacements of the crack [47,48]. The mode II SIF and COD values approaching the crack tip were also small, with mode I dominant, as the crack growth did not follow the inclined alignment of the notch. Under mixed mode loading, the development of the crack path depends on material, load magnitude, and also the initial crack tip condition [63]. As shown in Fig. 4, after initiating from the position of maximum tensile stress at the blunt notch tip, the cracks did not propagate parallel to the notch in the 30° configuration and tended to propagate in the vertical plane, perpendicular to the horizontal tensile stress induced by the vertical diametral compression. The cracks thus grew over a short distance in mixed mode I and II loading and then their path transitioned to experience mode I loading. This change in crack path is to be expected, as according to the minimum energy principle a crack will propagate in the direction where the energy dissipated is the minimum [64,65]. This demonstrates that the inclined central notch configuration in disc compression specimens is not an ideal geometry for investigating a range of mixed-mode conditions for propagating cracks, as the range of mode mixity that can be achieved is limited by the quite rapid change in crack path after initiation. Future studies, however, could achieve significant mode mixity, for example by rotation to the 30° configuration of specimens in which short cracks have been initiated in the 0° configuration.

For both SNG742 and T220, a strong increase in K_I for longer crack lengths (>3 mm propagation) in the 30° configuration can be observed in Fig. 12). This may be caused by the effect of distributed damage (i.e., microcracking) from the high contact stresses would invalidate the assumption of linear elasticity [66]. This would increase the measured strains and cause an apparent increase in the J-integral and SIFs that are calculated here with the assumption of linear elastic properties. It is noticeable that the crack lengths do not increase significantly with load once the crack exceeds ~3 mm length (Fig. 1c), which also suggests their propagation is affected by the limited change in stresses that would occur once damage developed at the specimen contacts. The crack geometry also becomes more complex, for instance in SNG742 under a load of 3294 N in the 30° configuration, when the crack is long (>3 mm propagation), the crack surface twists [Supplementary Information, section 4]), which is coincident with the slight increase of K_{II} and K_{III} [67]. Data for these longer crack lengths are therefore not considered to be representative of the material properties of the graphite.

The crack opening angles measured in this study were between 0.2° and 0.3°, with the larger value for SNG742. This is smaller than the opening angles of ~0.3–0.4° observed in DCDC specimens for the same graphites [68], and shows the crack opening angle is an indirect descriptor of the strain field ahead of the crack tip, as it depends also on the specimen geometry. The effect of crack extension on the specimen compliance would explain why the crack opening angle tended to increase with load, while the conditions at the crack tip, represented by K_I , remained constant (Figs. 9 and 12).

The cracks developed in a stable manner under quasi static loading, so the SIFs represent the critical conditions acting on the crack tip for crack propagation. In the 0° configuration, the constant K_I therefore describes the mode I fracture toughness, K_{IC} , and is higher for SNG742 than T220. This relative difference is consistent with literature data, which finds higher toughness for SNG742. The values obtained here are higher than data reported for standard specimen tests of both SNG742 and T220 [51,53]. However, the results of this study are close to those obtained in the same graphites using the mode I DCDC specimen geometry and the same finite element analysis method. In that study, which obtained K_{IC} of $1.54 \pm 0.16 \text{ MPa m}^{1/2}$ and $1.40 \pm 0.13 \text{ MPa m}^{1/2}$ for SNG742 and T220,

the boundary conditions were the displacement fields measured on the specimen surface by optical digital image correlation [68]. In both studies, the calculated toughness is an upper bound due to the assumption of linear elastic properties. The finite element analysis overestimates the strain energy release rate since it does not account for the non-linear properties of non-irradiated graphite. Tensile strain of virgin graphite causes microcracking and a reduction in the elastic modulus that reduces the stress at the crack tip [28]. Introducing a non-linear graphite damage model to the J-integral analysis can correctly calculate the crack stress field and strain energy release rate [24,28], but a calibrated damage model is currently only available for the coarse grained Gilsocarbon graphite [12].

To assess the potential effect of non-linear properties, the relationship between the elastic modulus and maximal principal strain reported previously for Gilsocarbon was used to estimate the nonlinear properties of SNG742 and T220 [Supplementary Information, section 5] and its effect was to decrease the J-integral under predominantly mode I conditions by ~35% [Supplementary Information, section 6]. Assuming the bulk elastic properties of the specimen are unchanged and the simple relationship $K = \sqrt{EJ}$, this reduction in the J-integral is equivalent to a reduction in K_I of ~20%, thus the values of K_{IC} extracted in the 0° mode I configuration for SNG742 and T220 may be reduced to $1.25 \pm 0.13 \text{ MPa m}^{1/2}$ and $1.15 \pm 0.11 \text{ MPa m}^{1/2}$. This is closer to the literature values obtained in standard specimens, and still shows the higher toughness of SNG742 compared to T220. A non-linear stress/strain relationship for unirradiated SNG742 and T220 that allowed better determination of the fracture toughness might be calibrated by approaches such as combined imaging/diffraction experiments [66], or inverse modelling [69]; the latter would be more suitable for routine testing and could be verified by the former. Inverse modelling with a linear elastic model could be sufficient for irradiated graphite as fast neutron irradiation increases the elastic modulus of graphite and removes its non-linear behaviour [24].

In summary, this study has shown that a constant mode I SIF is maintained at all positions at the tip of the curved crack during quasi-static propagation in fine-grained graphites, with no effect of the mode II SIF. This critical mode I SIF is an upper measure of the fracture toughness, as the current analysis assumes linear elastic behaviour. Introducing non-linear properties, which reduce the crack tip stress, provides mode I fracture toughness values that are consistent with literature data for larger standard specimens. SNG742 graphite has higher fracture toughness than T220 graphite. Under mixed mode loading, the crack propagates towards the path with maximum mode I SIF. Small specimen tests, such as the central-notched disc compression specimen with analysis of displacement fields, may be used to measure the fracture toughness of fine grained graphites. The observation that the mode II SIF has no effect on the mode I criteria for crack propagation may be significant both for the prediction of crack propagation paths [70] and also for estimation of the potential effects of internal defects from manufacture [71] on the strength of graphite components with multi-axial states of stress [72]. However, the current study only achieved a relatively small range of mode mixity, and further studies over a wider range are required to properly investigate the criteria for crack propagation under mixed mode loading.

5. Conclusion

Crack propagation in SNG742 and T220 graphites under nominal mode I and mixed modes I/II, has been investigated by tests of central-notched diametral compression specimens, observed in situ using X-ray micro-computed tomography. The characteristics

of the cracks, such as crack length, crack opening displacement and crack mouth opening displacement, were determined by a combined digital volume correlation and phase congruency analysis of the tomographs. The stress intensity factors and strain energy release rates were evaluated by linear elastic finite element simulations, using the measured 3D full field displacements as boundary conditions. This procedure for analysing the conditions of crack propagation is suitable for specimens and cracks of any shape, and is useful for small specimen tests in which complex crack shapes may develop.

For specimens loaded nominally in mixed mode I/mode II with a notch inclined at 30° to the diametral compression axis, the crack path deviated towards the vertical plane to develop mode I conditions at the crack tip. Evaluation of the crack tip stress intensity factors, with the assumption of linear elasticity, was performed under both nominal mode I and mixed mode loading as the crack propagated up to 3 mm. The mode I crack tip stress intensity factor, K_I , was effectively constant over this distance with no R-curve behaviour, and in these conditions where the crack tip mode II SIF was <20% of the mode I SIF, the crack propagation resistance was insensitive to the mixed mode loading. The higher mode I fracture toughness of SNG742 graphite relative to T220 graphite was demonstrated. The obtained values are an upper bound due to the assumption of linear elastic properties in the analysis.

CRedit authorship contribution statement

Xiaochao Jin: Investigation, Formal analysis, Software, Writing – original draft. **T. James Marrow:** Conceptualization, Methodology, Supervision, Writing – review & editing. **Jierui Wang:** Formal analysis. **Yang Chen:** Investigation, Software. **Hongniao Chen:** Investigation, Software. **Daniel Scotson:** Investigation, Software. **Boyuan Wang:** Formal analysis. **Houzheng Wu:** Resources. **Xueliang Fan:** Funding acquisition, Writing – review & editing, Supervision.

Declaration of competing interest

The authors declare that they have no known competing financial interests or personal relationships that could have appeared to influence the work reported in this paper.

Acknowledgement

This work is supported by National Science and Technology Major Project (J2019-IV-0003-0070). The facilities and software used for used for the X-ray tomography and digital volume correlation analysis were supported by EPSRC Grant EP/M02833X/1 “University of Oxford: experimental equipment upgrade”. X.C. Jin gratefully acknowledges the support of the National Natural Science Foundation of China (12102320) and China Postdoctoral Science Foundation (2021M692571). The graphite test specimens were kindly provided by Sinosteel.

Appendix A. Supplementary data

Supplementary data to this article can be found online at <https://doi.org/10.1016/j.carbon.2022.03.051>.

References

- [1] J.P. Bonal, A. Kohyama, J. Van Der Laan, L.L. Snead, Graphite, ceramics, and ceramic composites for high-temperature nuclear power systems, *MRS Bull* 34 (2009) 28–34.
- [2] B.J. Marsden, G.N. Hall, *Comprehensive Nuclear Materials*, Elsevier Ltd, 2012, pp. 325–390.
- [3] A.P.G. Rose, M.O. Tucker, A fracture criterion for nuclear graphite, *J. Nucl. Mater.* 110 (1982) 186–195.
- [4] R. Moskovics, P.E.J. Flewitt, E. Schlagen, G. Smith, A.G. Crocker, A. Hodgkins, P. Heard, M.R. Wootton, Understanding fracture behaviour of PGA reactor core graphite: perspective, *Mater. Sci. Technol.* 30 (2014) 129–145.
- [5] T. Abram, S. Ion, Generation-IV nuclear power: a review of the state of the science, *Energy Pol.* 36 (2008) 4323–4330.
- [6] S. Saito, T. Tanaka, Y. Sudo, Present status of the high temperature engineering test reactor (HTTR), *Nucl. Eng. Des.* 132 (1991) 85–93.
- [7] B.T. Kelly, Graphite the most fascinating nuclear material, *Carbon* 20 (1982) 3–11.
- [8] M. Mostafavi, S.A. McDonald, H. Çetinel, P.M. Mummery, T.J. Marrow, Flexural strength and defect behavior of polygranular graphite under different states of stress, *Carbon* 59 (2013) 325–336.
- [9] P.Y. Tang, Interpretation of bend strength increase of graphite by the couple-stress theory, *Comput. Struct.* 16 (1983) 45–49.
- [10] J. Brocklehurst, M. Darby, Concerning the fracture of graphite under different test conditions, *Mater. Sci. Eng.* 16 (1974) 91–106.
- [11] Y. Vertyagina, T.J. Marrow, A multi-scale three-dimensional cellular automata fracture model of radiolytically oxidised nuclear graphite, *Carbon* 121 (2017) 574–590.
- [12] T.J. Marrow, D. Liu, S.M. Barhli, L.S. Mora, Y. Vertyagina, D.M. Collins, C. Reinhard, S. Kabra, P.E.J. Flewitt, D.J. Smith, In situ measurement of the strains within a mechanically loaded polygranular graphite, *Carbon* 96 (2016) 285–302.
- [13] M.P. Hindley, D.C. Blaine, A.A. Groenwold, T.H. Becker, Failure prediction of full-size reactor components from tensile specimen data on NBG-18 nuclear graphite, *Nucl. Eng. Des.* 284 (2015) 1–9.
- [14] S. Yu, X. Fang, H. Wang, C. Li, Failure probability study of HTR graphite component using microstructure-based model, *Nucl. Eng. Des.* 253 (2012) 192–199.
- [15] ASTM International, ASTM D7779-11. Standard Test Method for Determination of Fracture Toughness of Graphite at Ambient Temperature, 2015. West Conshohocken, PA.
- [16] M.P. Metcalfe, N. Tzelepi, D. Wilde, Graphite Testing for Nuclear Applications: the Significance of Test Specimen Volume and Geometry and the Statistical Significance of Test Specimen Population, ASTM International, West Conshohocken, PA, 2014.
- [17] W.D. Carroll, M.C. Rohrbaugh, D.T. Chakraborty, P. Swank, Evaluating Alternate Test Techniques to Characterize Mechanical Properties in Nuclear-Grade Graphites, International Topical Meeting on High Temperature Reactor Technology, 2016, pp. 269–275.
- [18] A. Tzelepi, P. Ramsay, A.G. Steer, D.P. John, Measuring the fracture properties of irradiated reactor core graphite, *J. Nucl. Mater.* 509 (2018) 667–678.
- [19] C.G. Sammis, M.F. Ashby, The failure of brittle porous solids under compressive stress states, *Acta Metall* 34 (1986) 511–526.
- [20] J. Wade-Zhu, R. Krishna, A.J. Bodey, M. Davies, N.K. Bourne, C. Rau, B. Davies, A. Tzelepi, A.N. Jones, B.J. Marsden, P.M. Mummery, 4D synchrotron X-ray microtomography of fracture in nuclear graphite after neutron irradiation and radiolytic oxidation, *Carbon* 168 (2020) 230–244.
- [21] P. Ouagne, G.B. Neighbour, B. McEnaney, Crack growth resistance in nuclear graphites, *J. Phys. D Appl. Phys.* 35 (2002) 927–934.
- [22] T.H. Becker, T.J. Marrow, R.B. Tait, Damage, crack growth and fracture characteristics of nuclear grade graphite using the Double Torsion technique, *J. Nucl. Mater.* 414 (2011) 32–43.
- [23] A. Hodgkins, T.J. Marrow, P. Mummery, B. Marsden, A. Fok, X-ray tomography observation of crack propagation in nuclear graphite, *Mater. Sci. Technol.* 22 (2006) 1045–1051.
- [24] X.C. Jin, J. Wade-Zhu, C. Yang, P.M. Mummery, X.L. Fan, T.J. Marrow, Assessment of the fracture toughness of neutron-irradiated nuclear graphite by 3D analysis of the crack displacement field, *Carbon* 171 (2021) 882–893.
- [25] D. Singh, D.K. Shetty, Application of the method of caustics to the centre-cracked diametral compression test specimen, *J. Mater. Sci.* 23 (1988) 968–976.
- [26] C.F. Markides, D.N. Pazis, S.K. Kourkoulis, Stress intensity factors for the Brazilian disc with a short central crack: opening versus closing cracks, *Appl. Math. Model.* 35 (2011) 5636–5651.
- [27] A.F. Cinar, S.M. Barhli, D. Hollis, M. Flansbjerg, R.A. Tomlinson, T.J. Marrow, M. Mostafavi, An autonomous surface discontinuity detection and quantification method by digital image correlation and phase congruency, *Opt. Laser. Eng.* 96 (2017) 94–106.
- [28] S.M. Barhli, L. Saucedo-Mora, M.S.L. Jordan, A.F. Cinar, C. Reinhard, M. Mostafavi, T.J. Marrow, Synchrotron X-ray characterization of crack strain fields in polygranular graphite, *Carbon* 124 (2017) 357–371.
- [29] T.H. Becker, M.R. Molteno, T.J. Marrow, Procedure for accurate calculation of the J-integral from digital volume correlation displacement data, *Strain* 56 (2020), e12337.
- [30] M. Treifi, B.J. Marsden, G.N. Hall, P.M. Mummery, Keyway root crack arrest in an age graphite brick, in: 23rd Int Conf Struct Mech React Technol, 2015, pp. 1–48.
- [31] M. Wadsworth, S.T. Kyaw, W. Sun, Finite element modelling of the effect of temperature and neutron dose on the fracture behaviour of nuclear reactor graphite bricks, *Nucl. Eng. Des.* 280 (2014) 1–7.
- [32] J.D. Arregui-Mena, R.N. Worth, G. Hall, P.D. Edmondson, A.B. Giorla, T.D. Burchell, A review of finite element method models for nuclear graphite

- applications, *Arch. Comput. Methods Eng.* 27 (2020) 331–350.
- [33] M. Mostafavi, M.J. J. Schmidt, B.J. Marsden, T.J. Marrow, Fracture behaviour of an anisotropic polygranular graphite (PGA), *Mater. Sci. Eng.* 558 (2012) 265–277.
- [34] T.J. Marrow, M.S.L. Jordan, Y. Vertyagina, Towards a notch-sensitivity strength test for irradiated nuclear graphite structural integrity, in: 4th EDF Energy Nuclear Graphite Symposium Engineering Challenges Associated with Life Graphite Reactor Cores, Nottingham, UK, 2014, pp. 247–259.
- [35] A.R. Torabi, Sudden fracture from U-notches in fine-grained isostatic graphite under mixed mode I/II loading, *Int. J. Fract.* 181 (2013) 309–316.
- [36] A.R. Torabi, F. Berto, Strain energy density to assess mode II fracture in U-notched disk-type graphite plates, *Int. J. Damage Mech.* 23 (2014) 917–930.
- [37] M.R. Ayatollahi, F. Berto, P. Lazzarin, Mixed mode brittle fracture of sharp and blunt V-notches in polycrystalline graphite, *Carbon* 49 (2011) 2465–2474.
- [38] F. Berto, P. Lazzarin, C. Marangon, Brittle fracture of U-notched graphite plates under mixed mode loading, *Mater. Des.* 41 (2012) 421–432.
- [39] T. Wigger, B. Lin, C. Lupton, T.J. Marrow, J. Tong, A 3D full-field study of cracks in a nuclear graphite under mode I and mode II cyclic dwell loading conditions, *Fatig. Fract. Eng. Mater. Struct.* 43 (2020) 1646–1657.
- [40] M.R. Ayatollahi, M.R.M. Aliha, Mixed mode fracture analysis of polycrystalline graphite – a modified MTS criterion, *Carbon* 46 (2008) 1302–1308.
- [41] M.M. Mirsayar, F. Berto, M.R.M. Aliha, P. Park, Strain-based criteria for mixed-mode fracture of polycrystalline graphite, *Eng. Fract. Mech.* 156 (2016) 114–123.
- [42] A. Bahmani, M.R.M. Aliha, F. Berto, Investigation of fracture toughness for a polycrystalline graphite under combined tensile-tear deformation, *Theor. Appl. Fract. Mech.* 90 (2017) 53–64.
- [43] A. Ghazvinian, H.R. Nejati, V. Sarfarazi, M.R. Hadei, Mixed mode crack propagation in low brittle rock-like materials, *Arabian J. Geosci.* 6 (2013) 4435–4444.
- [44] D.K. Shetty, A.R. Rosenfield, W.H. Duckworth, Mixed-mode fracture in biaxial stress state: application of the diametral-compression (Brazilian disk) test, *Eng. Fract. Mech.* 26 (1987) 825–840.
- [45] H. Amrollahi, A. Baghbanan, H. Hashemolhosseini, Measuring fracture toughness of crystalline carbons under modes I and II and mixed mode I–II loading conditions using CCNBD and HCCD specimens, *Int. J. Rock Mech. Min.* 48 (2011) 1123–1134.
- [46] S. Ray, J.M.C. Kishen, Fatigue crack propagation model and size effect in concrete using dimensional analysis, *Mech. Mater.* 43 (2011) 75–86.
- [47] M.M. Mirsayar, F. Berto, M.R.M. Aliha, P. Park, Strain-based criteria for mixed-mode fracture of polycrystalline graphite, *Eng. Fract. Mech.* 156 (2016) 114–123.
- [48] W. Dong, D. Yang, B.S. Zhang, Z.M. Wu, Rock-concrete interfacial crack propagation under mixed mode I–II fracture, *J. Eng. Mech.* 144 (2018) 4018039.
- [49] T.D. Burchell, D. Erdmann, R.R. Lowden, J. Hunter, C. Hannel, The Fracture Toughness of Nuclear Graphite Grades (ORNL/TM-2016/678), 2016.
- [50] W. Lu, X. Li, X. Wu, L. Sun, Z. Li, Investigation on the oxidation behavior and multi-step reaction mechanism of nuclear graphite SNG742, *J. Nucl. Sci. Technol.* 57 (2020) 263–275.
- [51] Q. Huang, H. Tang, Porosity analysis of superfine-grain graphite IG-110 and ultrafine-grain graphite T220, *Mater. Sci. Tech-lond.* 35 (2019) 962–968.
- [52] H. Tang, Z. He, C. Zhang, X. Wang, H. Xia, Equipment design and experiment of compatibility test of nuclear graphite and molten salt, *He Jishu/Nuclear Techniques* 41 (2018) 70605, 070605.
- [53] Y. Gao, D.K.L. Tsang, Investigation on failure assessment method for nuclear graphite components, *Nucl. Eng. Technol.* 52 (2020) 206–210.
- [54] C. Hou, Z.Y. Wang, W.G. Liang, H.J. Yu, Z.H. Wang, Investigation of the effects of confining pressure on SIFs and T-stress for CCBD specimens using the XFEM and the interaction integral method, *Eng. Fract. Mech.* 178 (2017) 279–300.
- [55] C. Hou, Z.Y. Wang, X.C. Jin, X.K. Ji, X.L. Fan, Determination of SIFs and T-stress using an over-deterministic method based on stress fields: static and dynamic, *Eng. Fract. Mech.* 242 (2021) 107455.
- [56] M.R.M. Aliha, M.R. Ayatollahi, R. Pakzad, Brittle fracture analysis using a ring-shape specimen containing two angled cracks, *Int. J. Fract.* 153 (2008) 63–68.
- [57] S.M. Barhli, Advanced Quantitative Analysis of Crack Fields, Observed by 2D and 3D Image Correlation, Volume Correlation and Diffraction Mapping, University of Oxford, 2017. <https://ora.ox.ac.uk/objects/uuid:d6240241-8a1e-4a8e-aff0-4a2ef14b0da7>.
- [58] M. Sangsefidi, J. Akbaridoost, M. Mesbah, Experimental and theoretical fracture assessment of rock-type U-notched specimens under mixed mode I/II loading, *Eng. Fract. Mech.* 230 (2020) 106990.
- [59] Z.P. Bazant, M.T. Kazemi, Determination of fracture energy, process zone length and brittleness number from size effect, with application to rock and concrete, *Int. J. Fract.* 44 (1990) 111–131.
- [60] M.R. Ayatollahi, J. Akbaridoost, F. Berto, Size effects on mixed-mode fracture behavior of polygranular graphite, *Carbon* 103 (2016) 394–403.
- [61] A. Hodgkins, J. Marrow, P. Mummary, B. Marsden, A. Fok, L. Babout, Fracture behaviour of nuclear graphite[C], in: 2nd International Topical Meeting on High Temperature Reactor Technology, 2004, pp. 22–24.
- [62] D. Liu, B. Gludovatz, H.S. Barnard, M. Kuball, R.O. Ritchie, Damage tolerance of nuclear graphite at elevated temperatures, *Nat. Commun.* 8 (2017) 15942.
- [63] J. Qian, A. Fatemi, Mixed mode fatigue crack growth: a literature survey, *Eng. Fract. Mech.* 55 (1996) 969–990.
- [64] R.V. Gol'Dstein, R.L. Salganik, Brittle fracture of solids with arbitrary cracks, *Int. J. Fract.* 10 (1974) 507–523.
- [65] Q. Lin, X. Bian, P.Z. Pan, Y. Gao, Y. Lu, Criterion of local symmetry visualized in small eccentric single edge notched bend (E-SENB) rock specimens, *Eng. Fract. Mech.* 248 (2021) 107709.
- [66] D. Liu, T. Zillhardt, P. Earp, S. Kabra, T. Connolly, J. Marrow, In situ measurement of elastic and total strains during ambient and high temperature deformation of a polygranular graphite, *Carbon* 163 (2020) 308–323.
- [67] A. Kotousov, F. Berto, P. Lazzarin, F. Pegorin, Three dimensional finite element mixed fracture mode under anti-plane loading of a crack, *Theor. Appl. Fract. Mech.* 62 (2012) 26–33.
- [68] J. Marrow, D. Scotson, X.C. Jin, H.N. Chen, Y. Chen, A. Koko, P. Earp, H.Z. Wu, Small specimen testing, with image-based analysis, for crack propagation resistance in polygranular nuclear graphite, in: ASTM STP1639 Symposium on Graphite Testing for Nuclear Applications: the Validity and Extension of Test Methods for Material Exposed to Operating Reactor Environments, 2021.
- [69] G. Liu, L. Wang, Y. Yi, L. Sun, L. Shi, S. Ma, Inverse identification of graphite damage properties under complex stress states, *Mater. Des.* 183 (2019) 108–135.
- [70] Ł. Kaczmarczyk, Z. Ullah, C.J. Pearce, Energy consistent framework for continuously evolving 3D crack propagation, *Comput. Method, Appl. Mech. Eng.* 324 (2017) 54–73.
- [71] D.C. Kuerth, T.R. McJunkin, Nondestructive evaluation of nuclear-grade graphite, 45th annual review of progress in quantitative nondestructive evaluation, AIP Conf. Proc. 1430 (2012) 1609–1616.
- [72] D.K.L. Tsang, B.J. Marsden, Constitutive material model for the prediction of stresses in irradiated anisotropic graphite components, *J. Nucl. Mater.* 381 (2008) 129–136.